Multispectral Filter Array Design by Optimal Sphere Packing

Nelson Diaz, *Member, IEEE,* Alejandro Alvarado, *Student-Member, IEEE,* Pablo Meza, *Member, IEEE,*
Felipe Guzmán and Esteban Vera, *Member, IEEE*

Abstract—**Multispectral imaging (MSI) collects a datacube of spatio-spectral information of a scene. Many acquisition methods for spectral imaging use scanning, preventing its widespread usage for dynamic scenes. On the other hand, the conventional color filter array (CFA) method often used to sample color images has also been extended to snapshot MSI using a Multispectral Filter Array (MSFA), which is a mosaic of selective spectral filters placed over the Focal Plane Array (FPA). However, even state-of-the-art MSFAs coding patterns produce artifacts and distortions in the reconstructed spectral images, which might be due to the nonoptimal distribution of the spectral filters. To reduce the appearance of artifacts and provide tools for the optimal design of MSFAs, this paper proposes a novel mathematical framework to design MSFAs using a Sphere Packing (SP) approach. By assuming that each sampled filter can be represented by a sphere within the discrete datacube, SP organizes the position of the equal-size and disjoint spheres's centers in a cubic container. Our method is denoted Multispectral Filter Array by Optimal Sphere Packing (MSFA-OSP), which seeks filter positions that maximize the minimum distance between the spheres's centers. Simulation results show an image quality improvement of up to 2 dB and a remarkable boost in spectral similarity when using our proposed MSFA design approach for a variety of reconstruction algorithms. Moreover, MSFA-OSP notably reduces the appearance of false colors and zipper effect artifacts, often seen when using state-of-the-art demosaicking algorithms. Experiments using synthetic and real data prove that the proposed MSFA-OSP outperforms state-of-the-art MSFAs in terms of spatial and spectral fidelity. The code that reproduces the figures of this article is available at https://github.com/nelson10/DemosaickingMultispectral3DSpherePacking.git**

Index Terms—**Multispectral imaging, multispectral filter array, sphere packing, multispectral image demosaicing.**

I. INTRODUCTION

MULTISPECTRAL images are 3D signals with two spatial dimensions and several spectral bands. Multispectral imaging (MSI) has outstanding applications in remote

N. Diaz is with the School of Electrical Engineering, Pontificia Universidad Católica de Valparaíso, Valparaíso, Chile, e-mail: nelson.diaz@pucv.cl.

A. Alvarado is with the School of Electrical Engineering, Pontificia Universidad Católica de Valparaíso, Valparaíso, Chile, e-mail: alejandro.alvarado.v@mail.pucv.cl.

F. Guzman is with the School of Electrical Engineering, Pontificia Universidad Católica de Valparaíso, Valparaíso, Chile, e-mail: felipe.guzman.v@mail.pucv.cl.

P. Meza is with the Department of Electrical Engineering, Universidad de la Frontera, Temuco, Chile, e-mail: pablo.meza@ufrontera.cl.

E. Vera is with the School of Electrical Engineering, Pontificia Universidad Católica de Valparaíso, Chile e-mail: esteban.vera@pucv.cl.

sensing to classify materials such as ground, vegetation, and buildings in urban and rural areas [1]. In medicine, MSI provides diagnostic information about tissue morphology and physiology [2], allowing the detection of anomalies such as cancer tumors [3]. However, conventional methods to capture multispectral images rely on scanning–either spatial or spectral–to sample the whole datacube, also demanding larger bandwidth and storage. Scanning is also time-consuming and requires complex hardware, precluding to work with dynamic scenes. In contrast, novel snapshot methods inspired by the color filter array (CFA) can partially sample the datacube in a single acquisition, assuming that the whole datacube can be reconstructed by interpolation or more sophisticated algorithms that exploit spatial and spectral correlations.

The CFA acquires a sub-sampled version of the trichromatic spatio-spectral source in a 2D Focal Plane Array (FPA) [4]. Then, the captured grayscale mosaic image is used by demosaicking algorithms to reconstruct an approximation of the underlying RGB image. Similarly, a Multispectral Filter Array (MSFA) is a mosaic of spectral selective filters, often narrow bands, that extends the CFA approach to snapshot MSI. Specifically, MSFA acquires a single grayscale mosaic snapshot of the multispectral scene [5], where each pixel captures a particular spectral response of the corresponding spatial position; this snapshot approach is unique due to its compactness, low cost, and real-time features. Nevertheless, as a generalization of CFA, the design and use of MSFA poses several challenges. As more filters are considered, the sampling rate per channel is dramatically diminished, complicating the extension of traditional CFA demosaicking algorithms towards MSFA demosaicking. In contrast to many of the CFAs that have ad-Hoc design, such as the Bayer filter[4] that aimed to emulate the human visual system, one of the earliest mathematical models to design CFAs was proposed in 2008 [6], which uses the idea of 2D-sphere filling in the Fourier domain to maximize the radii of the luminance and chrominance channels subject to perfect reconstruction. Although this approach was initially focused on a few spectral filters for color imaging, it was extended later to MSFA [7] by using Fourier transform spectroscopy, leading to an efficient multispectral sensing modality that reduces stemming aliasing by exploiting multiplexed sinusoidal filters, leading to the design of 4×4 kernels with at most 16 different filters. Despite design efforts, conventional MSFAs such as binary tree-based edge-sensing (BTES) [5], Interuniversity Microelectronics Centre (IMEC) [8], [9] arrange the entries of the MSFA with arbitrary sampling patterns, which often

lead to artifacts in the reconstructed datacubes.

Therefore, we believe that the reconstruction problems in MSFA, regardless of the choice of demosaicking algorithm, arise due to the suboptimal sampling of the severely subsampled datacube. Hence, in this paper we proposed a novel, general mathematical framework to design regular MSFA coding patterns following a Sphere Packing (SP) approach exploiting Kepler's conjecture [10]. The SP method consists of packing congruent disjoint balls within a cubic container. We hypothesize that the spectral filters of a MSFA can be organized according to the SP approach; the analogy is as follows. The 3D position of the spectral filters corresponds to the sphere centers, the spatial resolution of the MSFA defines the cubic container size, and the number of filters coincides with the number of packed balls in the cubic container. We denote our approach as Multispectral Filter Array by Optimal Sphere Packing (MSFA-OSP) which has been successfully used for snapshot temporal imaging [11]. Our method maximizes the minimum distance between the spectral filters within the datacube, which can reduce not only artifacts such as color distortions in the demosaicked false color images but also the zipper effect. A striking feature when optimizing for equal size spheres is the reduction in the reconstructed distortions via uniform sampling. The regularity of the proposed coding patterns can improve the image reconstruction quality while making it straightforward to scale the MSFA demosaicking algorithms. Our proposed MSFA design makes the following contributions:

1) A general mathematical framework to model and optimize the MSFA as a SP problem. The optimal design maximizes the minimum distance between spectral filters of the MSFA. This framework provides an explanation of why state-of-the-art approaches such as Blue Noise (BN) Coded Aperture (CA) [12], [13], [14], MSFA-IMEC with 16 and 25 filters [8], [9], and MSFA-BTES with 16 filters [5], are nonoptimal (see Table I, and II; Fig. 4 and Fig. 5).
2) An algorithm to obtain the best parameters for the MSFA-OSP for any detector resolution (see Algorithm 1 and in Fig. 2). The proposed algorithm is highly competitive in computational time compared to other coding pattern design algorithms such as BN.
3) The proposed MSFA-OSP optimal coding patterns reduce reconstruction artifacts even when using conventional demosaicking algorithms (see Fig. 6, Fig. 7, and Fig. 8). For instance, the distortions introduced by using real spectral filter responses, such as in the IMEC camera, are also reduced using the proposed MSFA-OSP (see Table. II).
4) An adaptation to other state-of-the-art deep neural network (RevSCI [15])–already used in compressive spectral imaging applications–to the demosaicking/tensor completion problem in MSFA, enabling improved reconstructions for any MFSA pattern, also highlighting the superiority of the proposed MSFA-OSP designed patterns.

The remainder of this paper is organized as follows. In Sec. II, we introduce the previous art in multispectral demosaicking, snapshot compressive spectral imaging (CSI), and OSP. In Sec. III, we present the observation model of MSFA, the proposed SP approach using Optimal Sphere Packing (OSP), and the theoretical guarantees of the optimality of the proposed design. In Sec. IV, we provide simulations and experimental results of MSFA coding patterns and state-of-the-art demosaicking algorithms compared against our proposed SP approach.

II. RELATED WORKS

A. Reconstruction Methods

As an extension to demosaicking for the Bayer CFA, generalized demosaicking methods input the measured multispectral mosaic to recover the underlying spectral datacube. There are several demosaicking methods based on interpolation, intensity, spectral differences, and neural networks. One of the simplest demosaicking algorithms estimates the missing pixels using a weighted average of neighboring pixels, such as Weighted Bilinear (WB) interpolation [16], which was developed together with the Brauers (BRA) MSFA coding patterns. In a different approach, the scattered data interpolation method [17] uses a smoothing filter that exploits the spatial correlation, where the filter size is related to the smallest odd-size window that includes each channel at least once in the raw image. Among the spectral-difference-based methods, two techniques stand out. First, SD, which uses WB, exploits the spectral correlation and extends the approach to any arbitrary resolution with nonredundant MSFAs [16]. Second, Iterative Spectral Difference (ItSD) considers the correlation between two channels, which is high when the central wavelengths of the channels are close, improving over the SD method by updating the channel difference at each iteration [18]. The ID algorithm further combines the spatial and spectral correlations to estimate the missing values, interpolating the differences between the measured raw data and the estimated intensity values. A modification to ID has been proposed, such as the Iterative Intensity Difference (ItID) algorithm, which iteratively updates the intensity estimation using the previously estimated channel. Another modification is the Iterative Nearby Channel Difference (ItNCD) algorithm, which proposes iterating the ID algorithm by updating the intensity as an average over the spectrally closest channels rather than all channels, as in ItID. Specifically, the algorithm estimates the intensity difference for each channel using its previously estimated level and those of the two closest channels, outperforming previous demosaicking algorithms. Currently, there are also neural-network-based methods, such as the state-of-the-art method in [15], although it was originally developed for CSI problems. In contrast with CSI, the demosaicking problem in MSFA resembles a tensor completion problem more than the deconvolution problem related to compressive sensing. Therefore, we have also adapted [15] to our MSFA demosaicking problem, henceforth referred to as tensor reconstruction snapshot compressive imaging (TRevSCI).

B. Compressive Spectral Imaging

The MSFA has also been used in CSI to improve the encoding capability of classical architectures, such as coded aperture snapshot compressive imaging (CASSI). For instance, Rueda *et al.* successfully replaced the binary CA with an array of spectral filters entailing better encoding strategies in the colored coded aperture snapshot compressive imaging (C-CASSI) [19]. In 2015, Correa *et al.* introduced the snapshot colored compressive spectral imager (SCCSI) [20], which shears the spatio-spectral information using a prism. Then, an array of filters encodes the light before the FPA. Later, the spectral filter arrangement for CSI was optimized in [21], using the concentration of measure such that the optimal design satisfies the restricted isometry property (RIP). This approach minimizes the number of snapshots and maximizes the image quality; nevertheless, the approach still requires multiple shots and leads to nonuniform coding patterns, introducing distortions in the recovered datacubes. Another CA that satisfies the RIP is the BN coding pattern, which reduces many of the clusters of one-valued and zero-valued entries. Even so, some clusters inside the CA still harm its performance, and the algorithm that computes the coding patterns has a high computational cost [12], [13], [14]. In [22], another approach for colored CA tries to promote a more uniform sensing by keeping as uniform as possible, the distribution of the nonzero elements per column and row in the measurement matrix, although the density of the sampling is not completely uniform.

C. State-of-the-art MSFAs

We briefly describe seven state-of-the-art MSFAs. First, we have random (RND) coding patterns that are attained through random permutations of the filters within every kernel, or group of filters. Second, we use BN CA as another irregular coding pattern [12]. Third, we have the BRA MSFA that is used in combination with the WB algorithm to exploit the inter-channel correlation to compute the spectral differences [16]. Fourth, we have a sequential (SEQ) MSFA design, increasingly arranged row-by-row within a kernel. The fifth MSFA design, uniform (UNIF), exploits spectral consistency and spatial uniformity by enforcing that neighbor bands remain the same in all the array, while simultaneously achieving a regular sampling pattern for each filter [23]. Sixth, the IMEC-MSFA extends the basic Fabry-Pérot filter structure into a set of filters by varying the cavity length for each pixel-level filter within an $N \times N$ filter cell. They are embedded in a few off-the-shelf MSFA-based devices available on the market [8]. Seventh, the BTES MSFA generates patterns based on a binary tree, using a combination of decomposition and subsampling for any number of bands [5]. The subsequent subsection introduces the MSFA using SP.

D. Coded Aperture Optimization Using Sphere Packing

An outstanding problem in discrete geometry is SP [24], being closely related to coding theory and error-correcting codes [25] and with considerable applications in telecommunications and information theory [26]. In Euclidean space, SP consists of organizing the centers of equal size spheres within a cubic container such that the spheres remain disjoint or, at most, tangent between one another. Formally, Kepler's conjecture–recently demonstrated by Thomas Hales [27], [28]–establishes that face-centered cubic (FCC) lattice packing is the densest possible packing of equal spheres, which corresponds to $\eta = \frac{\pi}{3\sqrt{2}} \approx 0.74$ [10].

In the context of MSFA, the SP approach is equivalent to assigning a sphere to every spectral filter within a discretized spatio-spectral datacube that acts as the cubic container. Each sphere center is located at the spatial and spectral position of the corresponding spectral filter, considering that the spatial resolution of the MSFA in one dimension is equal to the number of distinctive filters within the MSFA to obtain a cubic container. The challenge of the SP problem relies on finding the optimal position of the sphere centers such that the spheres have a maximum size, which is equivalent to the spheres' centers being as far apart as possible from each other. A remarkable feature of the SP design is that congruent packing spheres guarantee uniform spatio-spectral sampling in the MSFA. Thus, solving for the SP problem leads to the optimization of the MSFA, which is analogous to a CA design. In 2022, a hardware modification to the rolling shutter (RS) mechanism found in complementary metal-oxide semiconductor (CMOS) detectors was presented by shuffling the pixels of the scanline, optimizing the position of the sampled pixels within the space-time datacube using SP [11]. The improved sampling scheme and novel reconstruction methods provided an alternative and efficient approach to snapshot temporal imaging. In this work, we adapt the design problem for the spatio-spectral datacube, mathematically model the CA design problem in MSFA as the SP problem that maximizes the minimum distance between the positions of the filters within the datacube. We call our design MSFA-OSP.

III. OPTIMIZATION STRATEGY

This section describes the continuous and discrete model, and the optimization strategy for the MSFA-based snapshot spectral imaging system.

A. Continuous Model

The encoded projections of the spectral component of the scene are captured as follows. As $f_0(u, v, \lambda)$ is the spatio-spectral source density, (u, v) is the index of spatial coordinates, and λ is the spectral coordinate, the MSFA transfer function is denoted as $C(u, v, \lambda)$. The coding is realized at the image plane creating the encoded datacube $f_1(u, v, \lambda) = C(u, v, \lambda)f_0(u, v, \lambda)$ that is integrated by the FPA detector, as depicted in Fig. 1(a). The integrated image along the spectral range sensitivity of the detector (Φ) can be written as

$$y(u, v) = \int_\Phi C(u, v, \lambda)f_0(u', v', \lambda)d\lambda. \tag{1}$$

Then, the coding transfer function of MSFA can be modelled as

$$C(u,v,\lambda) = \sum_{m,n,o} C_{m,n,o}\text{rect}\left(\frac{u}{\Delta_c} - m - \frac{1}{2},\right.$$
$$\left.\frac{v}{\Delta_c} - n - \frac{1}{2}, \frac{\lambda}{\Delta_d} - o - \frac{1}{2}\right), \quad (2)$$

where $C_{m,n,o} \in [0,1]$ denotes the filter operation in the $(m,n,o)^{\text{th}}$ datacube voxel; $m \in \{0,\ldots,M-1\}$, $n \in \{0,\ldots,N-1\}$, $o \in \{1,\ldots,O\}$ index the coordinates of an $M \times N \times O$ datacube, where M and N are the spatial resolution and O is the number of bands, while Δ_c, and Δ_d represent the pixel sizes of the CA and the FPA detector, respectively. Thus, the spatial and spectral resolution of the resolvable scene depends on the pitch size of the pixelated filters (Δ_c), the number of filters and the pixel pitch of FPA (Δ_d).

Assuming that ideal optical elements are used and that each voxel of the spectral scene is denoted as $X_{m,n,o} = \int\int\int_{\Psi_{m,n,o}} f_0(u,v,o)dudvdo = \omega_{m,n,o}f_0(u_m,v_n,o)$, where $\Psi_{m,n,o}$ denotes the $(m,n,o)^{\text{th}}$ voxel boundaries and $\omega_{m,n,o}$ the voxel mass center weight, then the measurement $(m,n)^{\text{th}}$ of the proposed system is given in discrete form by

$$Y_{m,n} = \sum_o X_{m,n,o}C_{m,n,o}, \quad (3)$$

being $m \in 0,\ldots,M-1$, $n \in 0,\ldots,N-1$ index the pixels in columns and rows on the detector, respectively.

B. Matrix Model

The acquisition of the spectral mosaic image projection of L spectral bands is

$$\mathbf{Y} = \sum_{o=1}^{O} \mathbf{X}_o \odot \mathbf{C}_o + \boldsymbol{\Omega}, \quad (4)$$

where $\mathbf{X}_o \in \mathbb{R}^{M \times N}$ is the oth spectral band of the datacube with $M \times N$ pixels, $\mathbf{C}_o \in \{0,1\}^{M \times N}$ is the binary CA and denotes the positions of the multispectral filters at the oth band, $\odot$ is the Hadamard product, and $\boldsymbol{\Omega} \in \mathbb{R}^{M \times N}$ is the Gaussian noise. Figure 1(b) depicts an example of the discrete model, where $\mathbf{X}$ denotes the multispectral datacube, $\mathbf{C}$ is the CA, and $\mathbf{Y}$ is the measurement.

C. Sphere packing background

This section introduces some of the basics concepts about SP. Overall, the SP problem is related to packing equal-sized spheres within a cubic container trying to minimize the void volume [24]. In general, SP can be mathematically defined by equivalent periodic structures or lattices [29]. An SP $\mathcal{P}$ is periodic if there is a lattice Λ such that $\mathcal{P}$ is invariant under translation by every element of Λ. A lattice in $\mathbb{R}^n$ is a discrete set of orthogonal vectors that can tile the n-dimensional Euclidean space. To compute the density of a lattice packing, it is convenient to view the lattice as a tiling of space with parallelotopes, which is the $n-$dimensional version of parallelograms. Lets define a basis $\mathbf{U} = [u_1,\ldots,u_n]$ for lattice Λ, therefore the parallelotope
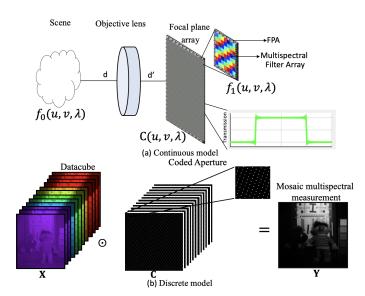

Fig. 1. Sketch of (a) the continuous and (b) discrete observation model of the MSFA.

$$\Lambda = \sum_{i=1}^{n} h_i u_i | h_i \in \mathbb{Z}, \quad (5)$$

is named the *fundamental cell* of Λ with respect to its basis, and it is also called the generator matrix. Thus, a lattice SP places spheres in the vertices of such a tiling, which is equivalent to having one sphere for each copy of the fundamental cell. Then, when the packing uses spheres of radius r and has a fundamental cell $\mathcal{F}$, then its density is the ratio

$$\frac{\text{Vol}(S_r^n)}{\text{Vol}(\mathcal{F})}, \quad (6)$$

where the two terms of the ratio are straightforward to compute if we are given r and $\mathcal{F}$. The volume of the fundamental cell is $\text{Vol}(\mathcal{F}) = \text{Vol}(\mathbb{R}^n/\Lambda) = \sqrt{\det(\mathbf{Q})}$, where $\text{Vol}(\mathbb{R}^n/\Lambda)$ is the volume of the quotient torus, in that case we avoid specifying the basis. The determinant of the matrix is $\det(\cdot)$, and the term $\mathbf{Q} = \mathbf{U}^T\mathbf{U}$ corresponds to the Gram matrix. The volume of an n-dimensional sphere of radius r in $\mathbb{R}^n$ is given by $\text{Vol}(S_r^n) = \frac{\pi^{n/2}}{(n/2)!}r^n$, where $(n/2)!$ means $\Gamma(n/2+1)$ when n is odd; note that Γ is a generalization of the factorial function. Thus, we can explicitly compute the volume of any lattice packing. For instance, the generator matrix for the best packing in 3D-SP is the FCC lattice

$$\mathbf{U}_3 = \begin{bmatrix} 1 & 1 & 0 \\ 1 & 0 & 1 \\ 0 & 1 & 1 \end{bmatrix},$$

where the Gram matrix is given by:

$$\mathbf{Q}_3 = \begin{bmatrix} 2 & 1 & 1 \\ 1 & 2 & 1 \\ 1 & 1 & 2 \end{bmatrix}.$$

Thus, the resulting FCC lattice density is

$$\frac{\mathrm{Vol}(S^3_{\frac{\sqrt{2}}{2}})}{\mathrm{Vol}(\mathbb{R}^3/\mathbf{U}_3)} = \frac{4\pi(\frac{\sqrt{2}}{2})^3}{3\sqrt{\det(\mathbf{Q}_3)}} = \frac{\pi}{\sqrt{18}}, \qquad (7)$$

where $r = \frac{\sqrt{2}}{2}$. Moreover, the density of a periodic packing is simple to compute if the packing is composed of V translates of a lattice $\Lambda \in \mathbf{R}^n$, whose sphere radius is r, as follows

$$\frac{V\,\mathrm{Vol}(S^n_r)}{\mathrm{Vol}(\mathbb{R}^n/\Lambda)}, \qquad (8)$$

then, extending the approach to V 3D-spheres contained in a cubic volume $(L+1)^3$,–whose side is $L+1$–fixes the density to $\frac{\pi}{\sqrt{18}}$. Therefore, by letting r and $\mathbf{U}$ to vary, we obtain that

$$\frac{V\,\mathrm{Vol}(S^3_r)}{(L+1)^3\mathrm{Vol}(\mathbb{R}^3/\mathbf{U})} = \frac{4V\pi r^3}{3(L+1)^3\sqrt{\det(\mathbf{Q})}} = \frac{\pi}{\sqrt{18}}. \quad (9)$$

Despite being optimal, the FCC lattice $\mathbf{U}_3$ may not always serve as a feasible solution given that the lattices might be subject to implementation restrictions. Therefore, in the next subsection we elucidate a novel method to find new implementable 3D lattices $\mathbf{U}$ with optimal radius r that fulfill the MSFA design constraints.

D. Multispectral Filter Array by Optimal Sphere Packing

The proposed 3D-SP approach to design the MSFA-OSP is based on packing equal spheres in a cubic container [30]. However, the grid restriction imposed by the use of discrete imaging detectors makes unfeasible to implement the optimal FCC lattices as a solution to design the MSFAs. Hence, we develop a novel procedure to design implementable MSFA-OSP patterns.

The majority of other MSFA designs use a square kernel of L nonoverlapping filters. Nevertheless, to account for the interaction between the filters beyond a single kernel in the design of the MSFA-OSP with L distinctive filters, we consider an expanded kernel having $V = L \times L$ filters, or spheres. This leads to a discretized datacube of $L \times L \times L$ voxels, where each of the V spheres centers are constrained to one of the L^3 discrete grid positions within the datacube.

From a similar application with spatio-temporal datacubes [11], we realized that we can arrive at optimal solutions to this class of constrained SP design problems by solving a related problem: the $3DN^2$ Queens Problem [31]–which is equivalent to finding the position of N^2 Queens within the N^3 slots of a 3D chess board without threatening one to another. We must emphasize that in our approach, we solve for a relaxed version of the $3DN^2$ Queens Problem by solely imposing strict uniformity in columns and rows, while allowing more degrees of freedom to the diagonals. Thus, the design of our MSFA-OSP can benefit from the following solution for the placement of the spheres within a kernel $\mathbf{B}$ as follows

$$\mathbf{B} = ((a \odot \mathbf{I} + b \odot \mathbf{J}) \mod L) + \mathbf{1}, \qquad (10)$$

being L is the number of spectral filters, $\mathbf{I} = \mathbf{g}^T \otimes \mathbf{q}$ such that $\mathbf{I} \in \mathbb{N}^{L \times L}$, $\mathbf{g}$ is a vector of all ones such as $\mathbf{g} \in \{1\}^L$, and $\mathbf{q} =$

$[1, \ldots, L]^T$ such as $\mathbf{q} \in \mathbb{N}^L$, $\odot$ denotes the Hadamard product, $\otimes$ represents the Kronecker product, $\mathbf{J} = \mathbf{I}^T$, $\mathbf{1} \in \mathbb{N}^{L \times L}$, $s, t \in \{1, \ldots, L\}$. Matrix $\mathbf{B} \in \mathbb{N}^{L \times L}$ can be reorganized as $\mathbf{p}_{k_1} = [s, t, B_{s,t}]$ such that $\mathbf{p}_{k_1} \in \mathbb{N}^z$ represents the centers of the $V = L^2$ spheres; this reorganization of pixels is exploited in Algorithm 1 to obtain the optimal parameters $a \in \mathbb{N}$ and $b \in \mathbb{N}$. Thus, the distance between a set of V spheres is given by

$$d^*(V) = \max(\min_{1 \le k_1 < k_2 \le V} D_{k_1,k_2}), \qquad (11)$$

where $k_1, k_2 \in \{1, \ldots, V\}$, such that $V = L^2$, $D_{k_1,k_2} = \|\mathbf{p}_{k_1} - \mathbf{p}_{k_2}\|_2^2$ is all pairwise distance matrix, thereby $\mathbf{p}_{k_1}$ and $\mathbf{p}_{k_2}$ are the centers of the k_1^{th} and k_2^{th} spheres, respectively (see [11]). The positions of the MSFA-OSP are given by

$$\mathbf{E} = \mathbf{A} \otimes \mathbf{B}, \qquad (12)$$

being $\mathbf{A}$ is a matrix of all ones such that $\mathbf{A} \in \{1\}^{\alpha \times \beta}$, where $\alpha = \lfloor \frac{M}{L} \rfloor$, and $\beta = \lfloor \frac{N}{L} \rfloor$, $\otimes$ denotes the Kronecker product, and $\mathbf{B}$ is computed using Eq. (10). The resulting positions of the MSFA can be expressed in a binary CA form as follows:

$$C_{m,n,l} = \begin{cases} 1 & \text{if } l = E_{m,n} \\ 0 & \text{if } l \ne E_{m,n}, \end{cases} \qquad (13)$$

where $m \in \{0, \ldots, M-1\}$, $n \in \{0, \ldots, N-1\}$ index the spatial coordinates, $l \in \{1, \ldots, L\}$ index the spectral filter coordinates, L being the number of filters of the MSFA.

E. Sphere Packing: Theoretical Upper Bound

In 2005, the proof of Kepler's conjecture proposed by Hales was accepted [27], [28]. The following statement is the resulting Theorem, which asserts that:

Theorem 1. *No packing of congruent balls in Euclidean three space has a density greater than that of the FCC lattice packing.*

This SP density is $\pi/\sqrt{18} \approx 0.74$. Leveraging theorem 1 and Eq. (9), besides knowing the volume of the V spheres, we infer the theoretical upper bound SP density for the optimal MSFA as

$$\rho^*(V) = 2\sqrt[3]{\frac{(\sqrt{V}+1)^3}{4V\sqrt{2}}}, \qquad (14)$$

being the OSP density is $\eta = \frac{\pi}{\sqrt{18}} = \frac{4V\pi r^3}{3(\sqrt{V}+1)^3} \approx 0.74$, note that for computing the upper bound, it is assumed that $V = MN$ according to Theorem 1, however, to compute MSFA, we use $V = L^2$. Fig. 2 depicts the theoretical upper bound of the SP density. In detail, the blue line, $\rho^*[V]$, represents the theoretical upper bound for the SP density computed using Eq. (14). The red line corresponds to the SP density $\rho_c[V]$ using continuous optimization [32], without the MSFA constraints. Finally, the green line corresponds to the SP density $\rho_i[V]$ with the MSFA constraint of using integer optimization.
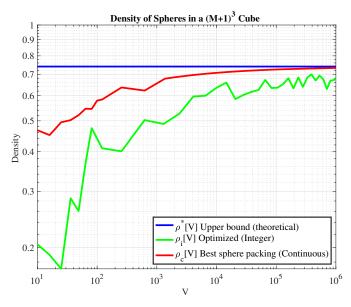
Fig. 2. SP density comparison for different dimensions; (blue line) theoretical upper bound where the cubic container has size $(M + 1)^3$, and the total number of spheres is $V = MN$; (red line) best known optimal sphere packing without the MSFA restriction; (green line) OSP density with MSFA restriction.

F. MSFA Analysis: Sphere's Diameter and Packing Density

The eight MSFAs coding patterns compared in this subsection are RND, BN CAs [12], BRA [16], SEQ, UNIF [23], MSFA-IMEC [8], MSFA-BTES [5], and the proposed MSFA-OSP. These MSFAs were described in subsection II-C; an example of the eight MSFAs are depicted in Fig. 3, where the spatial resolution corresponds to 16×16, and the number of filters is $L = 16$. Due to the limited space in this paper, we have provided the spatial distribution of the CA and more kernels with different of filters for our OSP in the Appendix A of the Supplementary Material. In addition, the improved spatio-spectral sampling is illustrated in Fig. 4, which compares the sphere's diameter d and the SP density ρ of 256 regular spheres using eight different MSFAs. The lower sphere's diameter is obtained with RND corresponding to 1, and the SP density is 0.03. Moreover, the sphere's diameter of the BN, BRA, SEQ, UNIF, and IMEC coding patterns is 1.41, and the corresponding SP density is 0.08, higher than the RND. In contrast, the sphere's diameter of BTES is 1.73. MSFA-OSP has the highest sphere's diameter of 2.44. It is clear that state-of-the-art MSFAs have a nonoptimized sphere's diameter, and the proposed SP approach promotes uniform spatio-spectral sampling in the MSFA. Moreover, the SP density of the RND is 0.03; for five state-of-the-art MSFAs is 0.08, and the BTES SP density is 0.14. All densities of state-of-the-art are lower than the SP density designed OSP coding patterns, which is 0.4.

Additionally, Fig. 5 shows the SP comparison between the traditional 5×5 IMEC coding patterns with 25 filters against MSFA-OSP. We include the corresponding MSFAs in the Appendix A of the Supplementary Material. Note that the number of spheres is 625. The nonoptimal IMEC coding patterns have a sphere's diameter of 1.41 and a SP density of 0.05. In contrast, MSFA-OSP has the largest sphere's diameter

of 3, and a corresponding SP density of 0.5. Note that the higher the SP density is, the better the uniformity of the sampling pattern, which improves the recovery of multispectral images with state-of-the-art demosaicking algorithms. In detail, demosaicking algorithms (see subsection II-A) provoke color distortions such as the zipper effect and false colors when nonoptimal state-of-the-art coding patterns are used. In contrast, our proposed optimal coding patterns avoid color distortions due to the optimized distance between filters and improved SP density, achieving better image reconstruction quality, as will be shown in Sec. IV in Fig. 7(e).

G. Parameters' Selection Algorithm

Note that putting different pairs of values to $a \in \mathbb{N}$ and $b \in \mathbb{N}$ in Eq. (10) produces different MSFA $\mathbf{B}$. Thus, our goal is to find the optimal values by conducting a smart search parameter space. The intuition that makes our algorithm faster than a brute force algorithm is the reduction of parameter pairs given symmetries found in the search space. Thus, algorithm 1, computes the optimal parameters by iteratively keeping the a and b, pairs that yield spheres with the largest diameter and thus, the best SP density. In detail, the input of the algorithm is the number of filters in the MSFA denoted by L, while the outputs are the parameters a and b that lead to the MSFA-OSP coding pattern. In stage 2 the constant K denotes the size of the search space of the possible solutions to Eq. (10). Line 3 assigns the number of spheres V to the MSFA kernel's size L^2. Lines 4 and 5 of Alg. 1 shows the initial values of a and b that span from 1 as the minimal value until K as the maximal value such that $i, j \in \{1, \dots, K\}$ being $K = \lfloor \frac{L}{2} \rfloor$. Different MSFA-OSP options that are plausible solutions to Eq. (10) are computed in line 6 by evaluating Eq. (10), with i and j entries at each iteration. Stage 8 promotes uniformity between the number of filters. If there is uniformity in $\mathbf{B}$, that means that the number of filters per column and row is the same, then all pairwise distances are computed, otherwise candidate $\mathbf{B}$ is ignored. In line 12, all the spheres' centers are stored in matrix $\mathbf{P} \in \mathbb{N}^{V \times 3}$. Then, in line 15, all the spheres' centers $\mathbf{P}$ are used to compute the pairwise distance matrix $\mathbf{D} \in \mathbb{R}^{V \times V}$, which stores the minimum distance of all the spheres ignoring the self-distance. Finally, in step 17, positions a and b correspond to the location of the maximum value of $\mathbf{W} \in \mathbb{R}^{K \times K}$. Note that solving the *max-min* problem in Eq. (11) implies computing steps 15 and 17 of Algorithm 1. The MSFA-OSP is computed with the parameters a and b solving Eq. (10) for the L spectral bands. In terms of computational complexity, Algorithm 1 generates a MSFA in an order of $\mathcal{O}(\frac{1}{8}L^4 z + \frac{2}{8}L^2)$.

IV. DEMOSAICKING RESULTS

A. Dataset Preparation and Evaluation Parameters

To verify MSFA-based sensor demosaicking, we use the CAVE dataset [33] to test the performance of MSFA-OSP against state-of-the-art MSFAs. The CAVE dataset consists of 32 scenes, with a spatial resolution of 512×512 and 31 spectral-bands, where the bandwidth is 10 nm between 400 nm and 700 nm. The dataset is resized to 256×256,
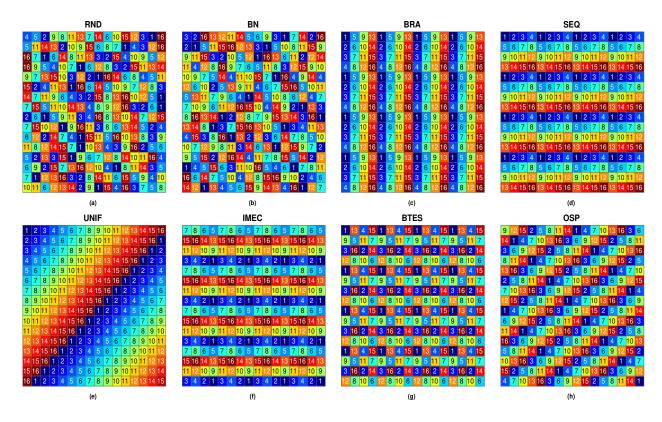
Fig. 3. Comparison between MSFAs with a spatial resolution of 16×16, and spectral resolution of 16. (a) RND, (b) BN, (c) BRA, (d) SEQ, (e) UNIF, (f) IMEC, (g) BTES, (h) OSP.
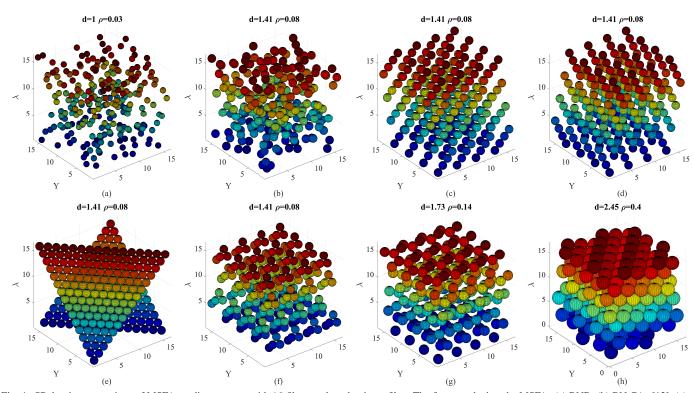

Fig. 4. SP density comparison of MSFAs coding patterns with 16 filters and no dominant filter. The first row depicts the MSFAs (a) RND, (b) BN CAs [12], (c) BRA [16], and (d) SEQ. The second row shows the MSFAs (e) UNIF, (f) IMEC [8], (g) BTES [5], and the proposed (h) MSFA-OSP computed using Eq. (12). State-of-the-art MSFAs experiments have corresponding sphere's diameter lower than the sphere's diameter of the OSP approach. The lower sphere's diameter is 1, with the SP density of 0.03 RND. Five state-of-the-art MSFAs have the same sphere's diameter and, therefore, the same SP density, corresponding to 1.41 and 0.08, respectively. The coding pattern BTES has sphere's diameter of 1.73 and a SP density of 0.14; the MSFA-OSP sphere's diameter is 2.44 and reaches a SP density of 0.4.
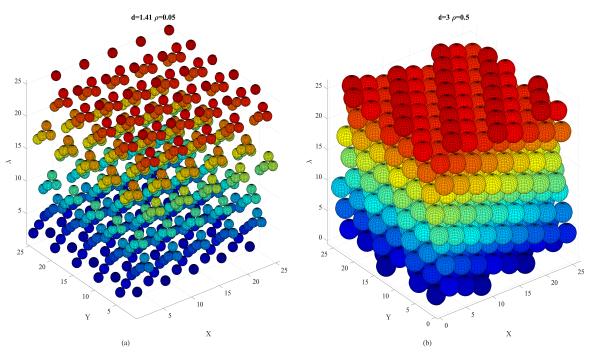
Fig. 5. SP density comparison using IMEC and OSP coding patterns. Two MSFA are compared (a) IMEC and (b) MSFA-OSP, both patterns have 25 filters with no dominant ones. The SP on the left depicts IMEC with kernel 5×5 with $L = 25$ [8], and the SP on the right shows the proposed MSFA-OSP computed using Eq. (12) with kernel 25×25. The corresponding IMEC sphere's diameter is lower than the diameter of the MSFA-OSP approach. The IMEC sphere's diameter is 1.41, and the SP density is 0.05; the sphere's diameter of MSFA-OSP is 3 and reaches a SP density of 0.5.

Algorithm 1 Selection of parameters a and b.

Input: L ▷ Input of the algorithm.
Outputs: a and b.   ▷ Outputs of the algorithm.
1:   **function** PARAMETER SELECTION(L)
2:      $K = \lfloor \frac{L}{2} \rfloor$ ▷ Compute the search space of the algorithm.
3:      $V = L^2$ ▷ Compute the number of spheres.
4:      **for** $i \leftarrow 1, K$ **do**
5:          **for** $j \leftarrow i, K$ **do**
6:              $\mathbf{B} \leftarrow$ **MSFA-SP**(i, j) ▷ Computes **B** Using Eq. (10).
7:              $q \leftarrow 0$
8:              **if** Uniformity($\mathbf{B}$)==true **then**   ▷ Promotes uniformity of the number of filters per columns and rows.
9:                 **for** $s \leftarrow 1, L$ **do**
10:                    **for** $t \leftarrow 1, L$ **do**
11:                       $q \leftarrow q + 1$
12:                       $\mathbf{p}_q \leftarrow [s, t, B_{s,t}]$ ▷ Center of qth sphere.
13:                 **for** $k_1 \leftarrow 1, V$ **do**
14:                    **for** $k_2 \leftarrow 1, V$ **do**
15:                       $D_{k_1,k_2} \leftarrow (\mathbf{p}_{k_1} - \mathbf{p}_{k_2})^T(\mathbf{p}_{k_1} - \mathbf{p}_{k_2})$ ▷ Computes all pairwise distance matrix different than 0.
16:              $W_{i,j} \leftarrow \min(\mathbf{D})$ ▷ The minimum distance is assigned.
17:      $a, b \leftarrow \operatorname{argmax}(\mathbf{W})$ ▷ Select a and b in **W** such that $W_{a,b}$ has the maximum value.
18:      **return** a and b ▷ Outputs of the algorithm.

---

either sub-selecting 16 interleaved spectral bands or sub-sets of sequential 25 bands, as needed for the different variations of the MSFA. Eight demosaicking algorithms are compared using the eight MSFAs coding patterns already introduced in Section II-C. Moreover, three quantitative metrics are used to assess the performance of the demosaicking algorithms. In order to measure the spatial fidelity, we use the Peak-Signal-to-Noise Ratio (PSNR) and the Structural Similarity Index (SSIM) [34], where high values of PSNR and SSIM stand for better spatial fidelity. We also use Spectral Angle Mapper (SAM) [35] to evaluate spectral similarity, where a lower SAM metric denotes better spectral fidelity.

B. Comparison between state-of-the-art MSFAs

We assess the following seven state-of-the-art MSFAs; RND, BN CAs [12], BRA [16], SEQ, UNIF [23], IMEC

[8], BTES [5] against our proposed MSFA-OSP. In particular, the MSFAs have a spatial resolution of 256×256 and the number of spectral filters are $L = 16$ or $L = 25$. In our evaluation, we use ideal dichroic filters and real filters with the spectral response taken from the IMEC [8], [9] camera, which is a unique off-the-self MSFA-based system available on the market. For additional information about the simulation experiments with real filters, see subsection IV-H. In addition, the designed MSFA-OSP coding patterns are computed using Eq. 12. The optimal a and b are selected using Algorithm 1, in which the corresponding values are $a = 7$ and $b = 4$ for 16 filters and $a = 8$ and $b = 3$ for 25 filters. The computation time of the MSFA-OSP coding patterns for the number of filters $L = 16$ is 0.08 seconds, and for the number of filters, $L = 25$ is 0.37 seconds. In contrast, BN may take several minutes to compute the coding patterns for a similar number of filters.

C. Neural Network Demosaicking Setup

The deep neural network that reconstructs the spectral datacube is a modification of the snapshot compressive imaging reconstruction called RevSCI [15]. We introduce the TRevSCI, which performs tensor completion using the grayscale multispectral mosaic $\mathbf{Y}$ computed with Eq. (4) for every specific CA $\mathbf{C}_l$. To ensure a fair comparison, we train eight different versions of the TRevSCI neural net using each one of the corresponding MSFA. An important difference between the original RevSCI and our TRevSCI is the loss function; we change the mean squared error (MSE) with the mean absolute error (MAE). Furthermore, for the training, we used four datasets: TokyoTech [36], Manchester [37], [38], Harvard [39], and ICVL [40]. These datasets contain 350 spectral datacubes that, through spectral and spatial data augmentation, are transformed into new 10530 datacubes, where 80% are used for training and 20% for validation. Then, we used the 32 datacubes from the Cave dataset [33] for testing. The neural network in our configuration is an autoencoder with two stages, comprising a set of 3D and 2D convolutional layers. Each convolutional layer is followed by a leaky ReLU activation layer, which has been shown to perform well in many snapshot computational imaging applications [11], [15], [41]. All experiments are run on the PyTorch framework with 2 NVIDIA RTX 3090 GPUs. The Adam optimizer [42] is used to minimize the loss function with a learning rate of 2×10^{-4}. It takes approximately a day and a half to train the entire network. For each experiment with every CA, the network was retrained using the same dataset with a specific MSFA.

D. Artifacts reduction analysis

To observe the performance of our novel approach in dealing with artifacts such as false color and the typical zipper effect, we test the state-of-the-art MSFAs IMEC and BTES against our OSP approach using the benchmarking chart scene of the Tokyotech [36] dataset (736×736 pixels and 16 spectral bands). In particular, Fig. 7(a) depicts the groundtruth of the chart scene, and Fig. 7(b-d) show the reconstructions using

IMEC, BTES and OSP, respectively. To better observe the zones with potential artifacts, we offer four zoomed versions of the scene highlighted with yellow, blue, red and green squares. The red squares of IMEC and BTES clearly show the appearance of the zipper effect, while our OSP approach show none. Moreover, squares blue, green and yellow depict false colorartifacts present in IMEC and BTES, while our approach is able to better handle this often common problem in MSFA demosaicking.

E. Comparison of Demosaicking Algorithms and State-of-the-Art MSFA

The simulation results using the CAVE [33] dataset for $L = 16$ spectral filters are depicted in Table I, showing quantitative average and standard deviation results over all 32 CAVE datacubes using spatial similarity and spectral fidelity. MSFA-OSP is compared against seven MSFAs coding patterns using eight state-of-the-art demosaicking algorithms, including TRevSCI. The best results are marked in bold. The best traditional demosaicking algorithm corresponds to ItNCD; nevertheless, it provokes line artifacts in the reconstruction (Fig. 7(d)). In contrast, TRevSCI outperforms conventional demosaicking algorithms in spatial resolution, spectral fidelity, and visual quality. Subsections IV-F and IV-G analyze the spatial reconstruction and spectral fidelity with examples. We include additional simulations results using different numbers of filters in the Appendix B of the Supplementary Material.

F. Spatial Fidelity Comparison

As the best performing MSFAs, Figure 7 compares the MSFA-BTES against our MSFA-OSP design in terms of image reconstruction quality using the PSNR metric. The first column in Fig. 7(a) depicts the RGB groundtruth of the thread spools, glass tiles, and paints scenes. From the second to the fifth column, the RGB spatial reconstruction is depicted using four of the most relevant tested demosaicking algorithms in terms of performance, that is, WB, ItID, ItNCD, and TRevSCI. According to the performance, the algorithms are sorted in ascending order from left to right. Note that our method outperforms MSFA-BTES in image quality at 2.58 dB, 2.83 dB, and 2.2 dB using the TRevSCI method. In the case of the reconstruction of the paints scene using the BTES coding pattern (in Fig. 7 rows 5th and 6th), there is a zipper effect in the white text. In the case of the thread spools and glass tiles datacubes (in Fig. 7 rows 1st to 4th), using TRevSCI and both MSFAs, the spatial structure is preserved. The difference in results is highlighted using the SAM metric in Fig. 8.

G. Spectral Similarity Comparison

Figure 8 compares the spectral fidelity using the SAM metric of the reconstructed datacubes using four state-of-the-art demosaicking algorithms. The test uses the best-performing two coding patterns, MSFA-BTES and MSFA-OSP. The first column in Fig. 8(a) shows the RGB groundtruth of the thread spools, glass tiles, and paints scenes. The spectral similarity is depicted for the different demosaicking algorithms, WB,
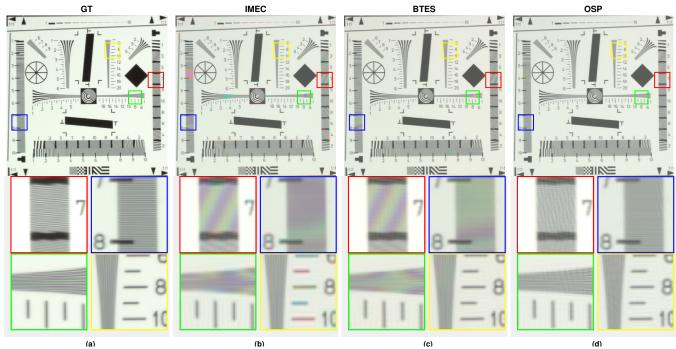
Fig. 6. Zipper effect and color distortion comparison between three MSFAs. The chart scene of Tokyotech [36] has a spatial resolution of 736×736 and 16 spectral bands, and the reconstruction algorithm is ItNCD, where (a) is the groundtruth (b) is IMEC, (c) is BTES, and (d) our proposed OSP approach. Four squares show zoomed versions of the scene; note the significant zipper effect and color artifacts in state-of-the-art patterns.

TABLE I
PERFORMANCE OF THE PROPOSED MSFA-OSP ON THE CAVE DATASET AGAINST SEVEN DIFFERENT MSFAS CODING PATTERNS, AND 8
DEMOSAICKING ALGORITHMS, WHERE $N = 256$, $L = 16$.

Algorithms	Metrics	MSFA coding patterns							
		UNIF	RND	BN	BRA	SEQ	IMEC	BTES	Ours
WB	PSNR (dB) ↑	17.06 ± 3.30	21.61 ± 3.33	22.99 ± 3.35	30.53 ± 3.56	30.50 ± 3.54	30.57 ± 3.59	30.53 ± 3.56	$\mathbf{30.72 \pm 3.57}$
	SSIM ↑	0.42 ± 0.17	0.61 ± 0.16	0.66 ± 0.16	0.89 ± 0.08	0.89 ± 0.08	0.89 ± 0.08	0.89 ± 0.08	$\mathbf{0.89 \pm 0.08}$
	SAM ↓	0.77 ± 0.02	0.49 ± 0.02	0.41 ± 0.02	$\mathbf{0.14 \pm 0.04}$	$\mathbf{0.14 \pm 0.04}$	0.14 ± 0.05	0.14 ± 0.05	0.14 ± 0.05
Interpolation	PSNR (dB) ↑	27.43 ± 3.42	29.76 ± 3.58	30.24 ± 3.59	30.53 ± 3.60	30.51 ± 3.60	30.45 ± 3.57	30.52 ± 3.61	$\mathbf{30.95 \pm 3.63}$
	SSIM ↑	0.81 ± 0.11	0.87 ± 0.09	0.88 ± 0.09	0.89 ± 0.08	0.89 ± 0.08	0.89 ± 0.08	0.89 ± 0.08	$\mathbf{0.89 \pm 0.08}$
	SAM ↓	0.19 ± 0.08	0.18 ± 0.07	0.17 ± 0.07	$\mathbf{0.15 \pm 0.06}$	0.16 ± 0.06	0.16 ± 0.06	0.16 ± 0.06	0.16 ± 0.07
ID	PSNR (dB) ↑	23.03 ± 3.82	27.79 ± 3.35	28.91 ± 3.32	32.27 ± 3.69	32.25 ± 3.66	32.33 ± 3.72	32.47 ± 3.73	$\mathbf{32.64 \pm 3.73}$
	SSIM ↑	0.65 ± 0.12	0.78 ± 0.10	0.81 ± 0.09	0.92 ± 0.06	0.92 ± 0.06	0.92 ± 0.06	0.92 ± 0.06	$\mathbf{0.92 \pm 0.06}$
	SAM ↓	0.43 ± 0.09	0.28 ± 0.05	0.24 ± 0.04	0.14 ± 0.04	0.14 ± 0.04	0.13 ± 0.04	0.14 ± 0.04	$\mathbf{0.13 \pm 0.04}$
SD	PSNR (dB) ↑	18.58 ± 3.43	22.25 ± 3.43	23.71 ± 3.39	32.30 ± 3.69	32.28 ± 3.67	32.34 ± 3.69	32.49 ± 3.69	$\mathbf{32.79 \pm 3.67}$
	SSIM ↑	0.48 ± 0.16	0.61 ± 0.16	0.65 ± 0.15	0.91 ± 0.05	0.91 ± 0.05	0.91 ± 0.05	0.91 ± 0.05	$\mathbf{0.92 \pm 0.05}$
	SAM ↓	0.71 ± 0.04	0.46 ± 0.03	0.40 ± 0.03	0.16 ± 0.05	0.16 ± 0.05	0.16 ± 0.05	0.16 ± 0.05	$\mathbf{0.15 \pm 0.05}$
ItSD	PSNR (dB) ↑	8.62 ± 0.53	14.44 ± 1.91	18.14 ± 2.55	32.96 ± 3.90	32.96 ± 3.83	33.05 ± 3.86	33.23 ± 3.86	$\mathbf{33.57 \pm 3.90}$
	SSIM ↑	0.09 ± 0.03	0.27 ± 0.10	0.45 ± 0.15	0.91 ± 0.06	0.91 ± 0.06	0.91 ± 0.06	0.91 ± 0.06	$\mathbf{0.92 \pm 0.05}$
	SAM ↓	1.03 ± 0.09	0.80 ± 0.05	0.60 ± 0.04	0.16 ± 0.05	0.16 ± 0.05	0.16 ± 0.05	0.16 ± 0.05	$\mathbf{0.15 \pm 0.05}$
ItID	PSNR (dB) ↑	22.03 ± 3.99	27.94 ± 3.53	28.90 ± 3.51	33.18 ± 3.83	33.14 ± 3.74	33.26 ± 3.78	33.88 ± 3.84	$\mathbf{34.03 \pm 3.83}$
	SSIM ↑	0.62 ± 0.13	0.78 ± 0.10	0.80 ± 0.09	0.92 ± 0.05	0.92 ± 0.05	0.92 ± 0.05	0.93 ± 0.05	$\mathbf{0.94 \pm 0.05}$
	SAM ↓	0.53 ± 0.12	0.30 ± 0.06	0.25 ± 0.05	0.14 ± 0.05	0.14 ± 0.05	0.14 ± 0.05	0.14 ± 0.04	$\mathbf{0.13 \pm 0.04}$
ItNCD	PSNR (dB) ↑	1.78 ± 0.60	31.99 ± 3.73	32.63 ± 3.74	34.51 ± 4.01	34.79 ± 3.79	35.11 ± 3.88	36.32 ± 4.00	$\mathbf{36.44 \pm 4.00}$
	SSIM ↑	0.01 ± 0.01	0.87 ± 0.06	0.88 ± 0.06	0.94 ± 0.04	0.94 ± 0.04	0.94 ± 0.04	0.95 ± 0.04	$\mathbf{0.95 \pm 0.05}$
	SAM ↓	0.70 ± 0.08	0.26 ± 0.07	0.24 ± 0.07	0.13 ± 0.04	0.14 ± 0.05	0.13 ± 0.05	0.13 ± 0.04	$\mathbf{0.13 \pm 0.04}$
TRevSCI	PSNR (dB) ↑	30.58 ± 3.99	34.95 ± 3.90	31.41 ± 3.65	31.83 ± 3.53	29.59 ± 3.33	35.81 ± 3.83	37.63 ± 4.15	$\mathbf{38.77 \pm 3.81}$
	SSIM ↑	0.89 ± 0.08	0.94 ± 0.05	0.88 ± 0.08	0.92 ± 0.06	0.92 ± 0.04	0.96 ± 0.04	$\mathbf{0.97 \pm 0.02}$	$\mathbf{0.97 \pm 0.02}$
	SAM ↓	0.18 ± 0.07	0.13 ± 0.06	0.20 ± 0.07	0.17 ± 0.05	0.24 ± 0.07	0.11 ± 0.04	0.11 ± 0.05	$\mathbf{0.11 \pm 0.04}$

ItID, ItNCD, and TRevSCI, in Fig. 8(b), (c), (d), and (e), respectively. The WB algorithm obtains blurred reconstructions increasing the SAM metric. ItNCD and ItID are comparable in terms of spectral similarity. The lowest spectral fidelity is attained using the TRevSCI algorithm, which outperforms the WB, ItID, and ItNCD demosaicking methods. In the three scenes, MSFA-OSP shows better spectral similarity than MSFA-BTES.

H. Results using real filters

In this section, we only compare MSFA-IMEC against MSFA-OSP. The ideal dichroic filters are replaced in both arrangements with the corresponding IMEC spectral filter responses. The TRevSCI neural network and MSFA with real filters are used to reconstruct the datacube. The real filters use the spectral response of the IMEC camera with 16 and 25 filters [8], [9]. Table II shows the corresponding results, where we note the superior performance of the MSFA-OSP design
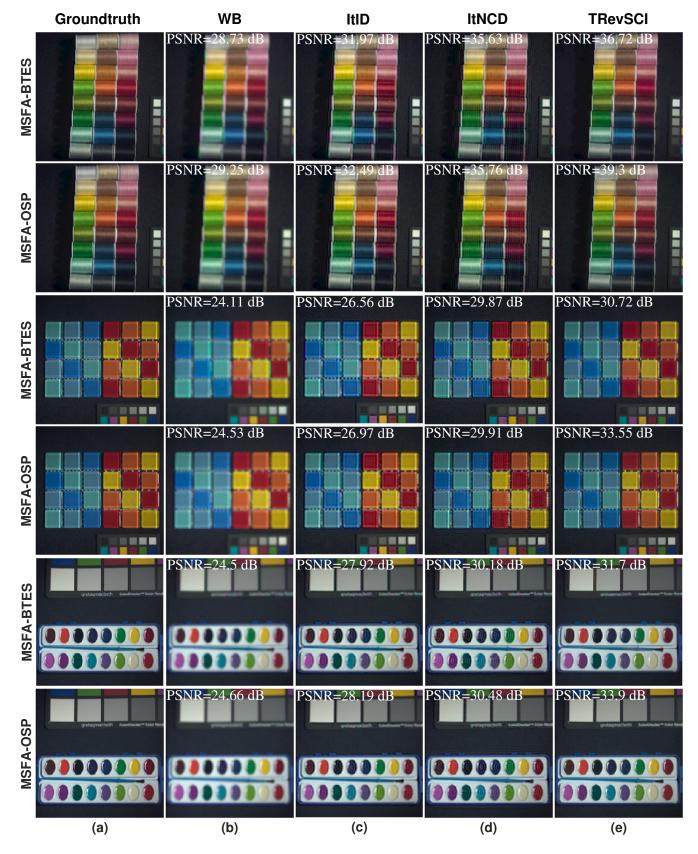
Fig. 7. Image quality reconstruction comparison using spatial fidelity. MSFA-OSP and MSFA-BTES are compared with three scenes: thread spools, glass tiles, and paints. The first column denotes (a) the original datacube, and subsequent columns depict reconstructions using four demosaicking methods (b) WB, (c) ItID, (d) ItNCD, and (e) TRevSCI. In the three scenes, the WB provokes a blurring in the reconstruction; ItID and ItNCD show line pattern artifacts. In contrast, TRevSCI recovers the details with high spatial fidelity and MSFA-OSP outperforms MSFA-BTES in terms of PSNR.
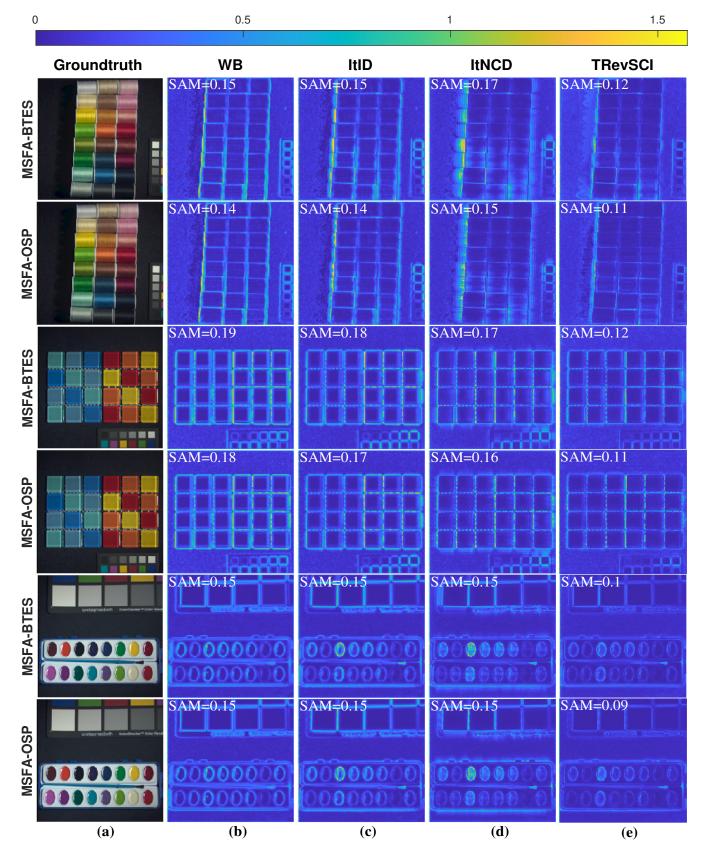
Fig. 8. Spectral fidelity comparison through the SAM metric of MSFA-BTES and MSFA-OSP using three scenes: thread spools, glass tiles, and paints. The first column shows the RGB original datacube. Moreover, the following columns show the spectral similarity using four demosaicking algorithms, (b) WB, (c) ItID, (d) ItNCD, and (e) TRevSCI.

TABLE II
PERFORMANCE OF MSFA-IMEC AGAINST THE PROPOSED MSFA-OSP
ON THE CAVE DATASET FOR TRevSCI NEURAL NETWORK, WHERE
$N = 256$, AND NUMBER OF FILTERS 16, AND 25. BOTH CODING
PATTERNS USE IMEC SPECTRAL FILTER RESPONSE.

Algorithm	MSFA	Number of filters	
		L=16	L=25
TRevSCI	IMEC PSNR (dB) ↑	35.05 ± 3.59	35.74 ± 3.97
	IMEC SSIM ↑	0.95 ± 0.03	0.95 ± 0.04
	IMEC SAM ↓	0.17 ± 0.07	0.17 ± 0.08
	OSP PSNR (dB) ↑	36.79 ± 3.92	37.36 ± 4.15
	OSP SSIM ↑	0.96 ± 0.03	0.96 ± 0.03
	OSP SAM ↓	0.16 ± 0.07	0.13 ± 0.06

for both numbers of filters. The advantage of our approach is that these results are obtained with a single snapshot compared to other approaches that even require several shots to attain a similar quality [9].

Moreover, an RGB visual comparison of spatial similarity is shown in Fig. 9, using MSFA-IMEC and MSFA-OSP coding patterns with real filters. In the experiment, three scenes are used. The first column in Fig. 9(a) shows an RGB version of the original images for the scenes thread spools, glass tiles, and paints. The second column in Fig. 9(b) and the third column in Fig. 9(c) depict the RGB reconstruction using 16 and 25 filters, respectively. The even rows correspond to MSFA-IMEC, and the odd rows correspond to MSFA-OSP. Note that PSNR is always lower for the IMEC coding pattern than for the MSFA-OSP with either number of filters.

Additional results are depicted in Fig. 10, where the spectral similarity between conventional MSFA-IMEC is compared against the proposed SP coding patterns using real filters. Fig. 10(a) (first column) depicts an RGB version of the original image. The second column in Fig. 10(b) and third column in Fig. 10(c) compare the spectral fidelity using 16 and 25 filters. Note that the SAM metric of the odd rows for MSFA-IMEC is comparable with MSFA-OSP for 16 filters and is higher when the number of filters is 25, which shows a better performance of our proposed approach.

I. Discussion

The experiments prove the capability of the MSFA-OSP to optimize the entries of MSFAs and reduce color artifacts, false color, and the zipper effect caused by the nonuniform sensing provided by the state-of-the-art MSFAs. In particular, BN CA is an optimized coding pattern such that the entries show cluster reduction in comparison with RND coding patterns. These patterns are used in CSI because they satisfy RIP; however, their spatial and spectral distribution are not optimal in terms of SP due to the irregular distribution of the sampling entries. Moreover, TRevSCI improved the reconstruction quality and leveraged the benefits of convolutional neural networks to boost spatial and spectral fidelity. It preserves fine details of the spectral bands by exploiting the spatial-spectral correlations to learn the structure of scenes that contrast with the interpolation and iterative demosaicking methods that cause significant distortions. A significant limitation of the proposed method is the necessity of retraining for specific MSFAs. Future work will include strategies to generalize MSFAs to avoid retraining for new MSFAs or exploit its scalability when the patter is
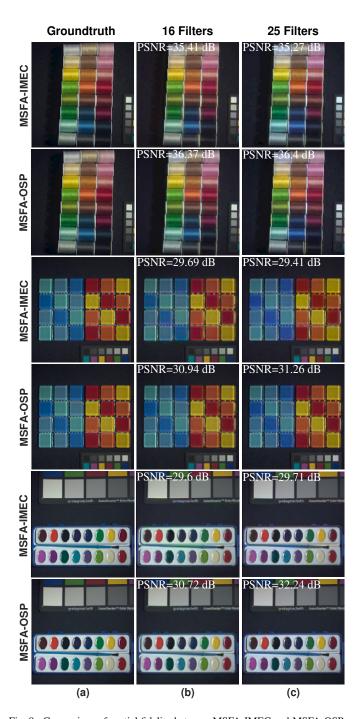

Fig. 9. Comparison of spatial fidelity between MSFA-IMEC and MSFA-OSP using real filters. For the experiment, the dichroic filters are replaced by the spectral response of the IMEC camera, and the reconstruction algorithm is TRevSCI. The first column in Fig. 9(a) shows the RGB groundtruth of three scenes thread spools, glass tiles, and paints. The second column in Fig. 9(b) and third column in Fig. 9(c) depict two different filter numbers, $L = 16$ and $L = 25$.
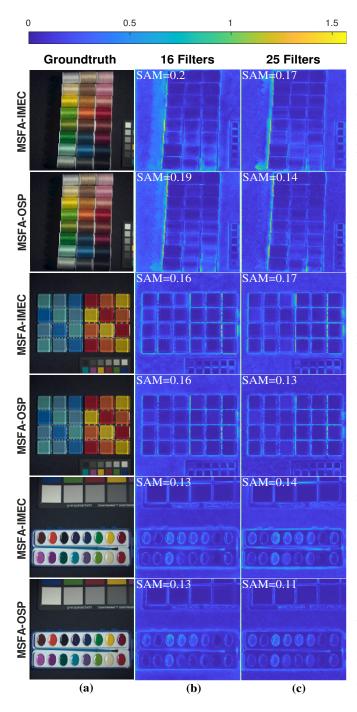
Fig. 10. A comparison of spectral similarity between MSFA-IMEC and MSFA-OSP using real filters means that the dichroic filters are changed for the spectral response of the IMEC camera, and the reconstruction algorithm is TRevSCI. The first column of Fig. 10(a) depicts the groundtruth of the thread spools, glass tiles, and paints of three scenes. The second Fig. 10(b), and third Fig. 10(c) columns show the spectral similarity of IMEC and OSP with 16 and 25 filters, respectively.

regular and thus repetitive. In addition, increasing the GPU memory will increase the number of reconstructed spectral bands.

V. CONCLUSION

We proposed a novel multispectral filter array design methodology for snapshot spectral imaging called Multispectral Filter Array by Optimal Sphere Packing (MSFA-OSP). The proposed approach exploits SP in 3D Euclidean space to optimally design the spatio-spectral coordinates of filters in an MSFA. The proposed SP approach extends the idea of optimal packing to optimal coded apertures design, generalizing the design of the MSFA for improved results. Simulation demonstrates that the MSFA-OSP outperforms in up to 2 dB seven state-of-the-art MSFAs; for instance, BN CAs and MSFA-BTES. In particular, our design is scalable to higher spectral dimensions via Algorithm 1, which calculates the optimal coding patterns for any filter number. Additional advantages of the optimal filter distribution are reducing artifacts in the reconstructed spectral datacubes, such as false colors and the typical zipper effect often found when using demosaicking algorithms. Simulations with spectral responses from real filters found in implemented Multispectral Filter Array (MSFA) prove that the proposed design outperforms the MSFA-IMEC coding patterns for 16 and 25 spectral filters. We believe that the improved performance achieved by the proposed Multispectral Filter Array by Optimal Sphere Packing (MSFA-OSP) has a correlation to the better SP density achieved in contrast with the MSFA-IMEC arrangement. In conclusion, the proposed SP optimization approach to designing a Multispectral Filter Array (MSFA) leads to regular and optimal sampling patterns that, at the end, allow the Multispectral Filter Array by Optimal Sphere Packing (MSFA-OSP) to retrieve the underlying spectral datacubes with better quality and fidelity no matter the reconstruction algorithm to be used, and even if the implemented filters are far from ideal.

The optimization using SP constitutes a general mathematical framework to optimize the spatial position of spectral filters in different areas, such as CSI, tomography and compressive videos. In CSI, we can further promote a regular distribution of colored filters in C-CASSI [21]. MSFA-OSP could also be exploited in compressive spectral X-ray imaging (CSXI) for optimal uniform illumination using K-edge CA [43]. Furthermore, the SP framework may be extended to CACTI to sample video frames using regular coding patterns [44]. For higher dimensions of the plenoctic function, we may consider studying the E_8 lattice [45], the Leech lattice [46], and the best known packing for Euclidean dimension, although the optimal SP is still only known for $2, 3, 8$ and 24 dimensions [24].

REFERENCES

[1] P. Ghamisi, J. Plaza, Y. Chen, J. Li, and A. J. Plaza, "Advanced spectral classifiers for hyperspectral images: A review," *IEEE Geoscience and Remote Sensing Magazine*, vol. 5, no. 1, pp. 8–32, 2017.

[2] G. Lu and B. Fei, "Medical hyperspectral imaging: a review," *Journal of Biomedical Optics*, vol. 19, no. 1, pp. 1–24, 2014. [Online]. Available: https://doi.org/10.1117/1.JBO.19.1.010901

[3] Q. Wang, L. Sun, Y. Wang, M. Zhou, M. Hu, J. Chen, Y. Wen, and Q. Li, "Identification of melanoma from hyperspectral pathology image using 3d convolutional networks," *IEEE Transactions on Medical Imaging*, vol. 40, no. 1, pp. 218–227, 2021.

[4] B. E. Bayer, "Color imaging array," *United States Patent 3,971,065*, 1976.

[5] L. Miao, H. Qi, R. Ramanath, and W. Snyder, "Binary tree-based generic demosaicking algorithm for multispectral filter arrays," *IEEE Transactions on Image Processing*, vol. 15, no. 11, pp. 3550–3558, 2006.

[6] K. Hirakawa and P. J. Wolfe, "Spatio-spectral color filter array design for optimal image recovery," *IEEE Transactions on Image Processing*, vol. 17, no. 10, pp. 1876–1890, 2008.

[7] J. Jia, K. J. Barnard, and K. Hirakawa, "Fourier spectral filter array for optimal multispectral imaging," *IEEE Transactions on Image Processing*, vol. 25, pp. 1530–1543, 4 2016.

[8] B. Geelen, N. Tack, and A. Lambrechts, "A compact snapshot multispectral imager with a monolithically integrated per-pixel filter mosaic," *Advanced Fabrication Technologies for Micro/Nano Optics and Photonics VII*, 2014.

[9] G. Tsagkatakis, M. Bloemen, B. Geelen, M. Jayapala, and P. Tsakalides, "Graph and rank regularized matrix recovery for snapshot spectral image demosaicing," *IEEE Transactions on Computational Imaging*, vol. 5, no. 2, pp. 301–316, 2019.

[10] J. Kepler, *The six-cornered snowflake*. Paul Dry Books, 2010.

[11] E. Vera, F. Guzmán, and N. Díaz, "Shuffled rolling shutter for snapshot temporal imaging," *Opt. Express*, vol. 30, no. 2, pp. 887–901, Jan 2022. [Online]. Available: http://opg.optica.org/oe/abstract.cfm?URI=oe-30-2-887

[12] C. V. Correa, H. Arguello, and G. R. Arce, "Spatiotemporal blue noise coded aperture design for multi-shot compressive spectral imaging," *J. Opt. Soc. Am. A*, vol. 33, no. 12, pp. 2312–2322, Dec 2016. [Online]. Available: http://opg.optica.org/josaa/abstract.cfm?URI=josaa-33-12-2312

[13] D. Lau, G. Arce, and N. Gallagher, "Digital color halftoning with generalized error diffusion and multichannel green-noise masks," *IEEE Transactions on Image Processing*, vol. 9, no. 5, pp. 923–935, 2000.

[14] J. Bacca Rodriguez, G. R. Arce, and D. L. Lau, "Blue-noise multitone dithering," *IEEE Transactions on Image Processing*, vol. 17, no. 8, pp. 1368–1382, 2008.

[15] Z. Cheng, B. Chen, G. Liu, H. Zhang, R. Lu, Z. Wang, and X. Yuan, "Memory-Efficient Network for Large-scale Video Compressive Sensing," *Proceedings of the IEEE Computer Society Conference on Computer Vision and Pattern Recognition*, pp. 16 241–16 250, 2021.

[16] J. Brauers and T. Aach, "A color filter array based multispectral camera," in *12. Workshop Farbbildverarbeitung*, G. C. Group, Ed., Ilmenau, October 5-6 2006.

[17] I. Amidror, "Scattered data interpolation methods for electronic imaging systems: a survey," *Journal of Electronic Imaging*, vol. 11, pp. 157–176, Apr. 2002.

[18] J. Mizutani, S. Ogawa, K. Shinoda, M. Hasegawa, and S. Kato, "Multispectral demosaicking algorithm based on inter-channel correlation," in *2014 IEEE Visual Communications and Image Processing Conference*, 2014, pp. 474–477.

[19] H. Rueda, H. Arguello, and G. R. Arce, "Dmd-based implementation of patterned optical filter arrays for compressive spectral imaging," *J. Opt. Soc. Am. A*, vol. 32, no. 1, pp. 80–89, Jan 2015. [Online]. Available: http://opg.optica.org/josaa/abstract.cfm?URI=josaa-32-1-80

[20] C. V. Correa, H. Arguello, and G. R. Arce, "Snapshot colored compressive spectral imager," *J. Opt. Soc. Am. A*, vol. 32, no. 10, pp. 1754–1763, Oct 2015. [Online]. Available: http://opg.optica.org/josaa/abstract.cfm?URI=josaa-32-10-1754

[21] H. Arguello and G. R. Arce, "Colored coded aperture design by concentration of measure in compressive spectral imaging," *IEEE Transactions on Image Processing*, vol. 23, no. 4, pp. 1896–1908, 2014.

[22] Y. Mejia and H. Arguello, "Binary codification design for compressive imaging by uniform sensing," *IEEE Transactions on Image Processing*, vol. 27, no. 12, pp. 5775–5786, 2018.

[23] H. K. Aggarwal and A. Majumdar, "Single-sensor multi-spectral image demosaicing algorithm using learned interpolation weights," in *2014 IEEE Geoscience and Remote Sensing Symposium*, 2014, pp. 2011–2014.

[24] J. H. Conway and N. J. A. Sloane, *Sphere packings, lattices and groups*. Springer Science & Business Media, 2013, vol. 290.

[25] R. W. Hamming, "Error detecting and error correcting codes," *The Bell System Technical Journal*, vol. 29, no. 2, pp. 147–160, 1950.

[26] C. E. Shannon, "A mathematical theory of communication," *The Bell System Technical Journal*, vol. 27, no. 3, pp. 379–423, 1948.

[27] T. C. Hales, "A proof of the kepler conjecture," *Annals of mathematics*, vol. 162, no. 3, pp. 1065–1185, 2005.

[28] T. Hales, M. Adams, G. Bauer, T. D. Dang, J. Harrison, H. Le Truong, C. Kaliszyk, V. Magron, S. McLaughlin, T. T. Nguyen, and et al., "A formal proof of the kepler conjecture," *Forum of Mathematics, Pi*, vol. 5, p. e2, 2017.

[29] H. Cohn, "A conceptual breakthrough in sphere packing," *Notices of the American Mathematical Society*, vol. 64, no. 02, pp. 102–115, feb 2017. [Online]. Available: https://doi.org/10.1090%2Fnoti1474

[30] M. Goldberg, "On the densest packing of equal spheres in a cube," *Mathematics Magazine*, vol. 44, no. 4, pp. 199–208, 1971. [Online]. Available: https://doi.org/10.1080/0025570X.1971.11976147

[31] L. Allison, C. Yee, and M. McGaughey, *Three-dimensional Queens Problems*. Monash University, Department of Computer Science, 1989.

[32] E. Specht, "Packomania," http://www.packomania.com/, 2008, (Accessed on 10/24/2022).

[33] F. Yasuma, T. Mitsunaga, D. Iso, and S. K. Nayar, "Generalized assorted pixel camera: Postcapture control of resolution, dynamic range, and spectrum," *IEEE Transactions on Image Processing*, vol. 19, no. 9, pp. 2241–2253, 2010.

[34] Z. Wang, A. Bovik, H. Sheikh, and E. Simoncelli, "Image quality assessment: from error visibility to structural similarity," *IEEE Transactions on Image Processing*, vol. 13, no. 4, pp. 600–612, 2004.

[35] F. Kruse, A. Lefkoff, J. Boardman, K. Heidebrecht, A. Shapiro, P. Barloon, and A. Goetz, "The spectral image processing system (sips)—interactive visualization and analysis of imaging spectrometer data," *Remote Sensing of Environment*, vol. 44, no. 2, pp. 145–163, 1993, airbone Imaging Spectrometry. [Online]. Available: https://www.sciencedirect.com/science/article/pii/003442579390013N

[36] Y. Monno, S. Kikuchi, M. Tanaka, and M. Okutomi, "A practical one-shot multispectral imaging system using a single image sensor," *IEEE Transactions on Image Processing*, vol. 24, no. 10, pp. 3048–3059, 2015.

[37] I. Marín-Franch and D. H. Foster, "Estimating information from image colors: An application to digital cameras and natural scenes," *IEEE Transactions on Pattern Analysis and Machine Intelligence*, vol. 35, no. 1, pp. 78–91, 2013.

[38] D. H. Foster and A. Reeves, "Colour constancy failures expected in colourful environments," *Proceedings of the Royal Society B: Biological Sciences*, vol. 289, no. 1967, Jan. 2022. [Online]. Available: https://doi.org/10.1098/rspb.2021.2483

[39] A. Chakrabarti and T. Zickler, "Statistics of real-world hyperspectral images," in *CVPR 2011*, 2011, pp. 193–200.

[40] B. Arad and O. Ben-Shahar, "Sparse recovery of hyperspectral signal from natural rgb images," in *European Conference on Computer Vision*. Springer, 2016, pp. 19–34.

[41] Z. Wu, J. Zhang, and C. Mou, "Dense deep unfolding network with 3d-cnn prior for snapshot compressive imaging," *arXiv preprint arXiv:2109.06548*, 2021.

[42] D. P. Kingma and J. Ba, "Adam: A method for stochastic optimization," in *ICLR (Poster)*, 2015. [Online]. Available: http://arxiv.org/abs/1412.6980

[43] T. Zhang, S. Zhao, X. Ma, A. P. Cuadros, and G. R. Arce, "K-edge coded aperture optimization for uniform illumination in compressive spectral x-ray tomosynthesis," *Opt. Express*, vol. 29, no. 25, pp. 41 048–41 066, Dec 2021. [Online]. Available: http://opg.optica.org/oe/abstract.cfm?URI=oe-29-25-41048

[44] P. Llull, X. Liao, X. Yuan, J. Yang, D. Kittle, L. Carin, G. Sapiro, and D. J. Brady, "Coded aperture compressive temporal imaging," *Opt. Express*, vol. 21, no. 9, pp. 10 526–10 545, May 2013.

[45] M. S. Viazovska, "The sphere packing problem in dimension 8," *Annals of Mathematics*, vol. 185, no. 3, pp. 991–1015, 2017. [Online]. Available: http://www.jstor.org/stable/26395747

[46] H. Cohn, A. Kumar, S. D. Miller, D. Radchenko, and M. Viazovska, "The sphere packing problem in dimension 24," *Annals of Mathematics*, vol. 185, no. 3, pp. 1017–1033, 2017. [Online]. Available: http://www.jstor.org/stable/26395748

Nelson Diaz (Member, IEEE) received the B.Sc.(Eng.) and M.Sc. in computer science engineering from the Universidad Industrial de Santander, in Colombia, in 2012 and 2015, respectively. During his Ph.D., he designed, simulated, and implemented adaptive systems for compressive spectral imaging for different tasks. Those tasks are hyperspectral and multispectral image classification, image reconstruction, and video sensing. He was under the supervision of Ph.D. Henry Arguello. He did an internship with Telecommunications for Space and Aeronautics Laboratory (TéSA), Toulouse, France, funded by Minciencias. During his internship, he developed a new algorithm for cardiac motion estimation in ultrasound imaging under the supervision of Ph.D. Jean-Yves Tourneret, and Adrian Basarab. His research topics are compressive spectral imaging, adaptive sensing, and video sensing. Currently, He holds a postdoctoral position at the Pontificia Universidad Católica de Valparaíso, (PUCV), Valparaíso, Chile. In his postdoc, He is developing sensing schemes for video and spectral acquisition under the supervision of Dr. Esteban Vera.

Esteban Vera (M'98) received the B.S. degree and Engineering diploma in electronics engineering, and the M.S. and Ph.D. degrees in electrical engineering from Universidad de Concepción, Concepción, Chile, in 1996, 1999, 2003, and 2010, respectively. From 2001 to 2007, he worked as an electronics engineer for different large telescope projects, first with the Paranal Observatory and then with the Gemini Observatory. In 2010, he was a postdoctoral research associate with the University of Arizona, Tucson, AZ, USA, and in 2013, he became a research scientist at Duke University, Durham, NC, USA. In 2016, he joined the School of Electrical Engineering, Pontificia Universidad Católica de Valparaíso, Valparaíso, Chile, where he is currently an associate professor. He leads the Optoelectronics Lab and his research interests span the fields of computational imaging, compressed sensing, inverse problems, signal processing, machine learning, and adaptive optics. He is an associate editor for the IEEE Open Journal on Signal Processing and Optics Express. He is a member of the SPIE and a senior member of OPTICA.

Alejandro Alvarado (S'20) received the B.Sc. and Engineering diploma in electronics engineering, in 2021, and the M.S. degree in electrical engineering, in 2022, Pontificia Universidad Católica de Valparaíso, Valparaíso, Chile. His research interests include signal and image processing, computational imaging, Deep Learning applications and image processing applied to spectral imaging systems. He is currently a Ph.D. student and a Lecturer professor for the School of electrical engineering, PUCV. He is a student member of the IEEE and OPTICA.

Pablo Meza was born on October 6, 1983. He received the B.Sc. degree in electronic engineering, in 2008, and the M.S. degree in electrical engineering, in 2008, from the University of La Frontera, Temuco, Chile, and the Ph.D. degree in electrical engineering from the University of Concepción, Concepción, Chile, in 2014. He is currently a Full-Time Professor with the Department of Electrical Engineering, University of La Frontera, Temuco, Chile. His research interests include signal and image processing applied to multi- and hyperspectral imaging systems.

Felipe Guzmán He received the B.Sc. degree in electronic engineering in 2018 and an M.S. degree in electrical engineering in 2019 from the Pontificia Universidad Católica de Valparaíso (PUCV), Valparaíso, Chile. He earned his master's degree working on the development of camera arrays for high-speed imaging. He has also taken several courses on adaptive optics and wavefront sensing at the Pontificia Universidad Católica de Chile and at the European AO Summer School. He is currently a Ph.D. student and a Lecturer professor for the School of electrical engineering, PUCV. His research interests include signal and image processing applied to hyperspectral and temporal imaging systems, machine learning and wavefront sensing. He is a member of the SPIE and member of the OSA, and he is a beneficiary of the national doctoral scholarship provided by the Agencia nacional de investigación y desarrollo (ANID).